JOURNAL OF PROPULSION AND POWER
Vol. 20, No. 3, May–June 2004

Asymmetric Base-Bleed Effect on Aerospike Plume-Induced Base-Heating Environment

Ten-See Wang,* Alan Droege,† Mark D'Agostino,‡ Young-Ching Lee,§ and Robert Williams¶
NASA Marshall Space Flight Center, Huntsville, Alabama 35812

A computational heat transfer design methodology was developed to study the dual-engine linear aerospike plume-induced base-heating environment during one power-pack out, in ascent flight. It includes a three-dimensional, finite volume, viscous, chemically reacting, and pressure-based computational fluid dynamics formulation, a special base-bleed boundary condition, and a three-dimensional, finite volume, and spectral-line-based weighted-sum-of-gray-gases absorption computational radiation heat transfer formulation. A separate radiation model was used for diagnostic purposes. The computational methodology was systematically benchmarked. In this study, near-base radiative heat fluxes were computed, and they compared well with those measured during static linear aerospike engine tests. The base-heating environment of 18 trajectory points selected from three power-pack out scenarios was computed. The computed asymmetric base-heating physics were analyzed. The power-pack out condition has the most impact on convective base heating when it happens early in flight. The source of its impact comes from the asymmetric and reduced base bleed.

Nomenclature

C_1, C_2, C_3, C_μ	=	turbulence modeling constants, 1.15, 1.9, 0.25, and 0.09
G	=	geometrical matrices
H	=	total enthalpy
h	=	static enthalpy
I	=	radiative intensity
J	=	Jacobian of coordinate transformation
K_f	=	forward rate constant
k	=	turbulent kinetic energy
M	=	Mach number
$\dot{m}_{bb}$	=	base-bleed mass flow rate, kg/s
N	=	total number of chemical species
P	=	pressure
PL	=	power level in percentage
Pr	=	Prandtl number
Q	=	heat flux, kW/m^2
q	=	$1, u, v, w, H, k, \varepsilon,$ or ρ_i
R	=	recovery factor
r	=	location coordinate
S_q	=	source term for equation q
T^+	=	law-of-the-wall temperature
t	=	time, s
U	=	volume-weighted contravariant velocity
u, v, w	=	mean velocities in three directions
u_τ	=	wall friction velocity
u^+	=	law-of-the-wall velocity, (u/u_τ)
x, y, z	=	coordinate or distance
y^+	=	law-of-the-wall distance, $(y_p u_\tau \rho/\mu)$
ε	=	turbulent kinetic energy dissipation rate or wall emissivity
κ	=	absorption coefficient
μ	=	effective viscosity, $(\mu_l + \mu_t)$
ξ	=	computational coordinates
Π	=	turbulent kinetic energy production
ρ	=	density
σ_q	=	turbulence modeling constants
φ	=	energy viscous source term
$\mathbf{\Omega}$	=	direction vector
ω	=	chemical species production rate

Subscripts

a	=	ambient
b	=	blackbody or base
c	=	convective or center
L	=	left engine or "on" engine
l	=	laminar flow
p	=	off-wall (wall function) point
R	=	right engine or "off" engine
r	=	radiative
t	=	turbulent flow
w	=	wall surface
0	=	reference

Introduction

THE X-33, a half-scale prototype of a proposed commercial, reusable launch vehicle was designed to demonstrate new, reusable single-stage-to-orbit technologies. It was fueled by liquid hydrogen and liquid oxygen and featured a lifting-body configuration coupled with two integrated, linear aerospike rocket engines. One goal of the project was to provide safe, reliable, and affordable access to space.

It is well known that aerospike engines have the potential advantage of adjusting themselves to perform with maximum efficiency at all altitudes.[1,2] However, the aerospike plume-induced, base-heating environments must be fully understood to satisfy safety and reliability requirements. One scenario of particular interest is the base-heating environment during a potential power-pack out (PPO), the loss of one of the two integrated turbopump sets, resulting in reduced power levels for both engines. This in turn reduces the amount of base bleed, which protects the plug-base components such as the pillows and flex seals (Fig. 1). The reduction of base bleed during PPO is a concern because heat-induced flex seal damage has been

Received 6 March 2003; revision received 5 September 2003; accepted for publication 10 September 2003.

*Expert Staff Consultant, Applied Fluid Dynamics Analysis Group. Senior Member AIAA.
†Engineer, Applied Fluid Dynamics Analysis Group.
‡Team Lead, Fluid Physics and Dynamics Group.
§Engineer, Fluid Physics and Dynamics Group.
¶Team Lead, Applied Fluid Dynamics Analysis Group. Senior Member AIAA.

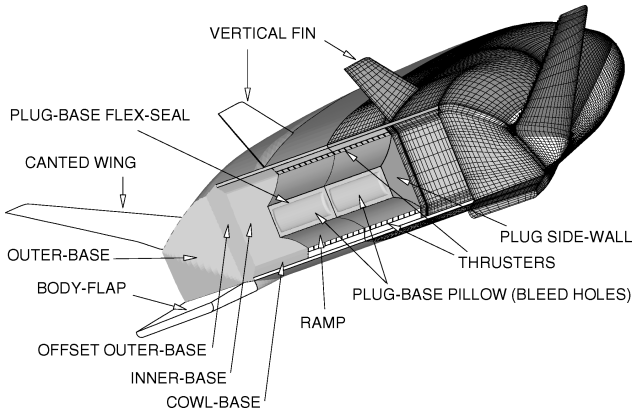

Fig. 1 Layout of an X-33 surface computational grid with component definitions.

observed after a single-engine, hot-fire test at reduced power levels. Furthermore, during PPO operation the on-engine side of the pillow receives about 75% of the remaining base bleed, whereas only 25% goes to the off-engine side. This creates a concern for the integrity of the plug-base components and the need to understand the physics and the impact of PPO on the ascent base-heating environment. Subscale testing is expensive, and combustion effects such as radiative heating are difficult to scale. Full-scale testing is not possible (because the risk of damaging an engine is not acceptable) and cannot adequately simulate altitude effect. Using anchored numerical tools to computationally simulate the base-heating environment during PPO is, therefore, a reasonable strategy to address these concerns and needs.

In the following sections, the computational methodology and the benchmarks performed are delineated first. The PPO trajectory and the run matrix are then discussed. Finally, the computational results showing the effect of base bleed on the base-heating environment during PPO are presented.

Solution Methodology

Computational Grid Generation

Previous studies[3,4] have shown that the X-33 base flowfield is three dimensional due to the linear aerospike layout and the lifting-body configuration. Only half of the domain was computed because flow symmetry can be assumed in normal operating conditions. In those studies, the computational grid was gradually improved through a sequential grid-refinement technique to an eventual number of 2,217,444 points.[3] Under PPO situations, the flow is asymmetric; hence, the flow over the entire vehicle is solved. The grid count is doubled to 4,434,888 points by mirror imaging the original half-vehicle grid using software package GRIDGEN.[5] Figure 1 shows a layout of the surface computational grid with component definitions. Notice the plug-base flex-seal region where severe base heating is expected after PPO. An identical grid is used in the radiation calculation. The total grid number is increased to 4,724,592 points, however, due to the cell-centered scheme used by the radiation solver as opposed to the node-centered scheme employed by the flow solver.

Flow and Radiation Computation

The effect of base bleed on the X-33 base-heating environment is investigated with two computational tools. For convective heating, the finite difference Navier–Stokes (FDNS) computational fluid dynamics (CFD) code[6] was used, and for radiative heating, the General Radiation Solution Program (GRASP)[7] was used. These tools were developed and are continuously being improved by NASA Marshall Space Flight Center (MSFC) personnel and supporting contractors. Systematic and rigorous benchmark studies have been performed for base flow and heat transfer applications. For example, FDNS has been validated for convective heat transfer inside rocket thrust chambers[8] and coolant channels,[9] for base-pressure characterization of a four-engine clustered nozzle configuration,[10,11] for Delta Clipper-Experimental (DC-X) base drag induced by the engine exhaust during cold-flow and flight tests,[12] and for DC-X convective base-heat flux during landing.[13] GRASP has been benchmarked for DC-X radiative base-heat flux during landing.[13] In this study, FDNS and GRASP calculations are conducted sequentially to save computational memory. The CFD computed pressure, H_2O concentration, and temperature fields are inputs for the radiation calculations. The solution algorithm for the flow and radiation computation is summarized in the following.

Flow Solution and Convective Heat Transfer

FDNS solves a general curvilinear coordinate, chemically reacting, viscous thermoflowfield with Reynolds-averaged transport equations. A generalized form of these equations is given by

$$\frac{\partial \rho q}{J\,\partial t} = \frac{\partial \lfloor -\rho U q + (\mu/\sigma_q) G(\partial q/\partial \xi)\rfloor}{\partial \xi} + \frac{S_q}{J} \tag{1}$$

A pressure-based predictor-plus-multicorrector solution method is applied.[14] The basic idea is to perform correction for the pressure and velocity fields by solving for a pressure correction so that the velocity–pressure coupling is enforced, based on the continuity constraint. A second-order, central-difference scheme is employed to discretize the diffusion fluxes and source terms of the governing equations. For the convective terms, a second-order, total-variation-diminishing difference scheme is used in this effort.

An extended k–ε turbulence model[15] is used to describe the turbulence. Here $\mu_t = \rho C_\mu k^2/\varepsilon$ is defined as the turbulence eddy viscosity. Turbulence modeling constants σ_q and source terms S_q of the transport equations are given in Table 1. These turbulence modeling constants have been used extensively for combustion-driven and base flows,[8–14,16] whereas σ_k and σ_ε are taken from the turbulence closure.[15] A seven-species, nine-reaction detailed mechanism[16] (Table 2) is used to describe the finite rate, hydrogen–oxygen afterburning chemical kinetics. The seven species are H_2, O_2, H_2O, O, H, OH, and N_2, where H_2O is the major radiating medium. Although it has been shown that the importance of afterburning chemical kinetics diminishes at high altitudes during full-power flight,[3] the finite-rate chemistry is turned on for all of the trajectory points in this study due to considerations of reduced power level and base bleed during PPO.

A modified wall function approach is employed to provide wall boundary-layer solutions that are less sensitive to the near-wall grid

Table 1 Transport equations σ_q and S_q

q	σ_q	S_q
1	1.00	0
u	1.00	$-P_x + \nabla[\mu(u_j)_x] - (2/3)(\mu \nabla u_j)_x$
v	1.00	$-P_y + \nabla[\mu(u_j)_y] - (2/3)(\mu \nabla u_j)_y$
w	1.00	$-P_z + \nabla[\mu(u_j)_z] - (2/3)(\mu \nabla u_j)_z$
H	0.90	$\partial P/\partial t + \varphi$
k	0.89	$\rho(\Pi - \varepsilon)$
ε	1.15	$\rho(\varepsilon/k)\{[C_1 + C_3(\Pi/\varepsilon)]\Pi - C_2\varepsilon\}$
ρ_i	0.90	$\omega_i, i = 1, \ldots, N$

Table 2 Hydrogen–oxygen combustion kinetics mechanism, $K_f = AT^B \exp(-E/RT)$

Reaction	A	B	E/R
$H_2 + O_2 = OH + OH$	$1.700E13$	0	$2.407E4$
$OH + H_2 = H_2O + H$	$2.190E13$	0	$2.590E3$
$OH + OH = O + H_2O$	$6.023E12$	0	$5.500E2$
$O + H_2 = H + OH$	$1.800E10$	1.0	$4.480E3$
$H + O_2 = O + OH$	$1.220E17$	−0.91	$8.369E3$
$M^a + O + H = OH + M$	$1.000E16$	0	0
$M + O + O = O_2 + M$	$2.550E18$	−1.0	$5.939E4$
$M + H + H = H_2 + M$	$5.000E15$	0	0
$M + H + OH = H_2O + M$	$8.400E21$	−2.0	0

[a]M stands for third-body collision partner.

spacing. Consequently, the model has combined the advantages of both the integrated-to-the-wall approach and the conventional law-of-the-wall approach by incorporating a complete velocity profile[17] given by

$$u^+ = \ell_n\left[(y^+ + 11)^{4.02}\Big/\left(y^{+^2} - 7.37y^+ + 83.3\right)^{0.79}\right] + 5.63\tan^{-1}(0.12y^+ - 0.441) - 3.81 \quad (2)$$

and a universal temperature profile[18] given by

$$T^+ = u^+ + 12.8\left(\mathrm{Pr}_l{}^{0.68} - 1\right) \quad (3)$$

The convective heat transfer follows the modified Newtonian law (see Ref. 13),

$$Q_{cw} = \left(\rho u_\tau / T^+\right)\left\lfloor h_w - h_p - R\left(u_p^2/2\right)\right\rfloor \quad (4)$$

where $R = Pr_l^{1/2}$ if $y^+ \le 11.63$ and $R = Pr_l^{1/3}$ if $y^+ > 11.63$, and $y^+ = 11.63$ is the thickness of the viscous sublayer. A constant Prandtl number Pr_l of air is used because parametric studies performed in Ref. 13 show that the H_2–O_2 plume-induced base heat flux is not sensitive to a multicomponent variable Prandtl number Pr_l.

Radiative Heat Transfer

GRASP analyzes the radiative field by solving the general curvilinear coordinate radiative transfer equation with a finite volume method formulation,[19]

$$(\Omega \cdot \nabla) I(r, \Omega) = -\kappa I(r, \Omega) + \kappa I_b(r) \quad (5)$$

The term on the left-hand side represents the gradient of the intensity in the direction of Ω. The two terms on the right-hand side represent the changes in intensity due to absorption and emission. The wall boundary is assumed gray while emitting and reflecting diffusely, and the radiative wall boundary condition is given by

$$I(r_w, \Omega^+) = \varepsilon I_b(r_w) + \frac{(1-\varepsilon)}{\pi} \int_{n\cdot\Omega^- < 0} I(r_w, \Omega^-)|n \cdot \Omega^-| \mathrm{d}\Omega^- \quad (6)$$

with

$$Q_{rw} = \int_{n\cdot\Omega^- < 0} I(r_w, \Omega^-)|n \cdot \Omega^-| \mathrm{d}\Omega^- \quad (7)$$

where Ω^+ and Ω^- are the leaving and arriving radiative intensity directions, respectively. The 20-band spectral-line weighted-sum-of-gray-gases model[7] is used to calculate the total emissivity and absorptivity of the radiating medium. Following the ray-dependency test performed in Ref. 13, the finite volume method 6×4 option (six control angles in the polar direction and four in the azimuthal direction) is deemed adequate and is used in this effort.

Boundary and Initial Conditions

The outer boundaries of the computational domain have the fixed total-condition (freestream) and the flow exit plane. A no-slip wall is specified for the body surface. A fixed (ambient) static pressure is imposed on the exit plane and on a point far away from the action area (one grid point off the freestream boundary), to obtain a unique solution for the desired altitude. The fixed inlet boundary condition is applied to the exit plane of the 40 thrusters where the flow properties were obtained from a chemical equilibrium analysis using the CEC code.[20]

Base bleed is accomplished in the actual engines by flowing a mixture of hydrogen gas and steam from thousands of orifices drilled on the pillows. Because it is computationally prohibitive to resolve all of the individual orifices in the CFD model, the orifices and the pillow surface surrounding them can be lumped together and modeled as one base bleed inlet boundary. In Refs., 3 and 4, a fixed mass flow rate (and energy) boundary condition is used in subsonic freestream cases, and a fixed inlet boundary condition is applied in supersonic freestream cases. This approach, however, precludes the calculation of convective heat flux on the pillow because it is treated as an inlet and not a wall. In this study, a special base bleed boundary treatment is devised by combining the features of constant mass flow injection normal to the surface and those of wall boundary treatment such that the increased convective heating due to reduced base bleed can be estimated for subsonic freestream cases. For supersonic freestream cases, the pillow convective heating is negligible, and the fixed inlet boundary condition is retained. The basic assumptions for the base bleed boundary treatment are that the injection is always normal to the wall surface and the total mass flow rate specified is constant throughout the computation. In the mean time, the local mass flow rate is allowed to change in response to the change in local flow environment. Constant injection temperature and species composition are imposed to maintain a fixed inlet enthalpy. Because the base-bleed boundary is treated partially as a wall, the wall function approach is applied, and the wall heat flux can be estimated. Figure 2 shows the computed initial base-bleed flow vectors at 40 s into the PPO at the launch +30-s trajectory. Note that the flow vectors (mass flow rate) of the off-engine side are about one-third the length of those of the on-engine side.

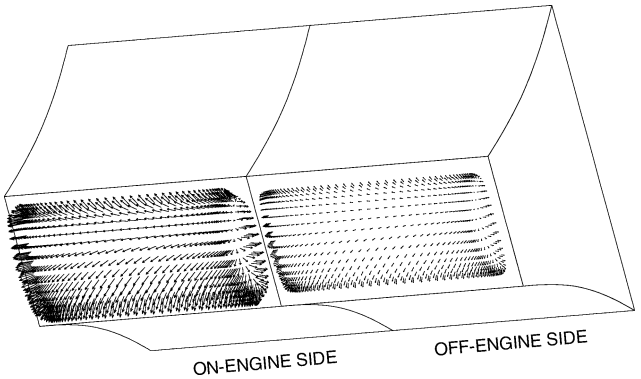

Fig. 2 Computed initial base-bleed flow vectors at 40 s into PPO at launch +30-s trajectory.

For convective heat transfer calculations, ambient temperature is prescribed as the forebody and aftbody surface temperatures, whereas 540°R is specified for all base surfaces per base-heating design convention. For radiation calculations, the surface emissivity of the entire vehicle is assumed to be 0.7 (Ref. 13). The engine ramp is actively cooled, and the surface temperature distribution is prescribed from a separate conjugate heat transfer calculation involving solid walls and coolant channel flows. It was found[3] that cowl-base irradiation is more than 10 times higher if an adiabatic condition is imposed on the ramp surface. Hence, a more accurate boundary condition is employed. Notice that the effect of reirradiation from surface radiation is included in all calculations.

Aerospike Engine Specific Computational Benchmarks Performed

Forebody and Aftbody Surface Pressure Coefficients

The X-33 forebody and aftbody surface pressure coefficients were computed, and they compared reasonably well with those of a 7.75% scaled model cold-flow test.[3] These comparisons indicate that the incoming flow environment is adequately simulated for X-33 base-flow development.

Installed Linear Aerospike Engine Plume-Induced Noise

The X-33 CFD plume database[3] was used in conjunction with an engineering acoustic radiation model to predict the acoustic environment[21] of the linear aerospike engine. This prediction was then compared with that measured from a series of hot-fire tests. The predicted far-field acoustic spectra, directivity pattern, and overall sound pressure levels agreed reasonably well with those of

measurement. Because the acoustic radiation model uses CFD computed $(\partial u/\partial n)^{-1}$, (k/ε), and (k/Π) for time scaling, this benchmark indicates the CFD computed X-33 plume velocity and turbulence fields are appropriate.

Base-Pressure Characteristic Curves

The base-pressure characteristic curve is the central base pressure plotted as a function of ambient pressures. The computed base-pressure characteristic curve[3,4] was compared with that of a 7.75% scaled model cold-flow test[3] and that of a 2.25% scaled model hot-flow test.[22] The agreement indicates that the predicted base-pressure characteristic curve is reasonable.

Sea-Level Base Pillow Pressures

The computed sea-level base pillow pressures[4] agreed reasonably well with those of a 2.25% scaled model hot-flow test.[22] The predicted and measured pressure levels indicate there is a strong aspiration occurring on the base pillow at low altitudes.

Base Horizontal Centerline Convective Heat Fluxes

Base horizontal centerline convective heat fluxes were computed and compared with those of a 2.25% scaled model hot-flow test at sea level, at 23.4 km, and at 23.4 km with fences installed.[4] The measurements[22] were made on the plug base, side wall, inner base, offset outer base, and outer base. Not only is the predicted convective base heating in good agreement with experimental data, the linear aerospike base-heating physics such as the formation of the reverse jet, lateral wall jet, plume spillage, and aspiration jet are well captured.

Installed Linear Aerospike Engine Plume-Induced Base Radiative Heat Fluxes

Radiation predictions were made using FDNS flowfield solutions with heating rates generated by the GASRAD code.[23] The GASRAD code uses a statistical band model for exponential line strength distribution with Lorentz/Doppler line shapes for gaseous species. Its geometry model provides high-fidelity integration over a hemisphere and can accept either axisymmetric or three-dimensional plumes. GASRAD is particularly well suited for very accurately predicting radiation to individual geometry points, whereas GRASP is typically used for entire surface predictions due to its relatively high computational efficiency. Near-base radiative heat fluxes were computed and compared with those measured from a series of hot-fire tests of a single X-33 XRS-2200 linear aerospike engine at the NASA Stennis Space Center in 1999 and 2000.

Wideband plume radiation data were collected during the XRS-2200 test series. Plume radiation instrumentation consisted of several 180-deg hemispherical radiometers. A typical view of the engine and plume during test is shown in Fig. 3. Wide-angle (180-deg) radiometer locations were selected to provide orientations similar to that of flight vehicle surfaces and flight test instruments. Most instruments, for example, radiometer R101B (Fig. 4), were located to the side parallel to the engine long axis in what would be the engine base region. One radiometer, radiometer R105 (Fig. 5), was in close proximity to the engine near the cowl base and thruster area on the ramp side.

The FDNS solutions were generated at sea-level ambient pressure. Ground-test radiation data are compared to sea-level predictions in Figs. 4 and 5. Predicted steady-state levels agree quite well with those of measured data. Temporal variation of the data is due to engine startup and shutdown transients, as well as scheduled power level and oxidizer/fuel (O/F) mixture ratio changes.

Some additional insight into modeling accuracy can also be gained from these data. Radiometer R101B has a view factor encompassing a large potion of the engine plume. The fact that the predicted level agrees well with the data as shown in Fig. 4 gives us confidence that the overall plume flowfield is being modeled accurately. In addition, Fig. 5 shows that data from the cowl base region radiometer R105 are also reasonably predicted. This indicates that the local flowfield just downstream of the engine thrusters is being

Fig. 3 XRS-2200 engine test.

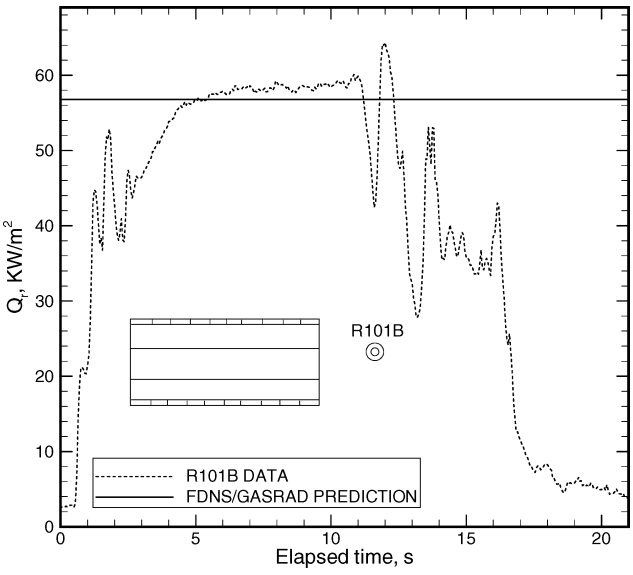

Fig. 4 Comparison of radiative heat fluxes for radiometer R101B.

modeled accurately because the field of view of radiometer R105 covers mostly that region. The results of these benchmarks validate our computational heat transfer model for studying the X-33 aerospike plume-induced base-heating environment during PPO.

PPO Trajectories and Run Matrix

The linear aerospike plume-induced X-33 base-heating environment was computed for trajectory points selected from three PPO scenarios: PPO at launch +30 s, PPO at launch +60 s, and PPO at launch +120 s. The ascent mission was expected to fail if PPO occurs before launch +30 s. Figure 6 shows the computational points selected on the thrust, altitude, and Mach number profiles for those three PPO trajectories. Six strategic points were selected for each trajectory to bracket the base-heating environment. Note that one

point was chosen before the PPO and another point was chosen after the PPO. This is best illustrated in thrust profiles because the biggest power difference occurred right after the PPO. To save computational time, several selected points were overlapped on the three PPO trajectories. For example, the trajectory points of 0 and 30 s on the PPO at launch +60-s trajectory are identical to those of 0 and 30 s on the PPO at launch +30-s trajectory. This way, the original number of computational points of 18 is reduced to 13. Tables 3–5 show the engine and base-bleed parameters of the computational points for those three PPO trajectories. The power levels of the dual engines at selected trajectory points were provided, whereas the base-bleed mass flow rates on the two pillows were estimated based on the 75/25 split for engine-off cases. During PPO, for example, at 40 s into the PPO at launch +30-s trajectory (Table 3), the power levels (PL) of both engines drop from about 100% (at 30 s) to about 50%. The total base bleed also drops 50%, and the resulting base bleed mass flow rate on the off-engine side is only about one-third of that of the on-engine side. Note that the power levels, mixture ratios (O/F), and the base bleed mass flow rates are slightly different for the dual engines at all points of the trajectories.

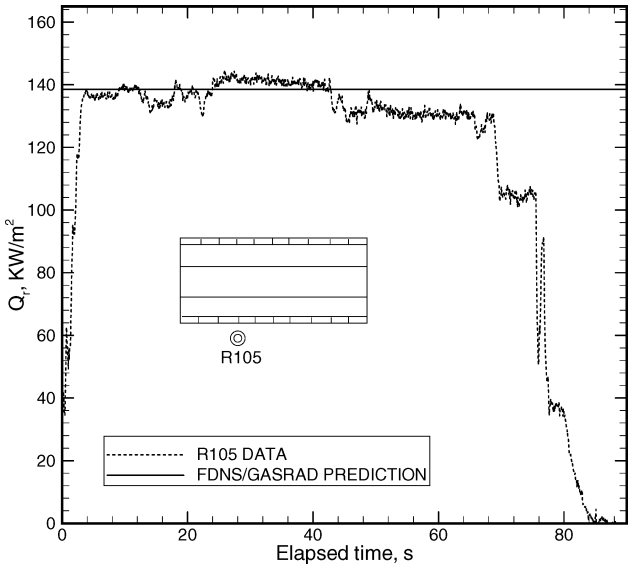

Fig. 5 Comparison of radiative heat fluxes for radiometer R105.

Results and Discussion

The flow computations were performed on a NASA MSFC Silicon Graphics Power Challenge cluster using eight processors. The computational time for a typical calculation is 4.5×10^{-5} CPU s/grid/step/processor. Usually, 2000–6000 iterations are required to achieve an approximate convergence. The radiation computations were performed on a NASA Ames Research Center Silicon Graphics

Table 3 Computational parameters for PPO at launch +30-s trajectory

t, s	PL_L	PL_R	O/F_L	O/F_R	$\dot{m}_{bb,L}$	$\dot{m}_{bb,R}$
0	81	79	5.7	5.4	4.5	4.4
30	99	100	5.6	5.6	5.4	5.5
40	49	48	5.7	5.4	4.1	1.3
100	49	49	5.5	5.6	4.1	1.3
200	51	48	5.6	5.7	4.1	1.3
280	45	40	6.1	5.8	3.6	1.1

Table 4 Computational parameters for PPO at launch +60-s trajectory

t, s	PL_L	PL_R	O/F_L	O/F_R	$\dot{m}_{bb,L}$	$\dot{m}_{bb,R}$
0	81	79	5.7	5.4	4.5	4.4
30	99	100	5.6	5.6	5.4	5.5
60	72	74	5.6	5.7	3.9	4.1
61	37	39	4.6	4.9	3.2	1.0
200	50	48	5.3	5.7	4.1	1.3
270	42	41	5.4	5.6	4.4	1.1

Table 5 Computational parameters for PPO at launch +120 s trajectory

t, s	PL_L	PL_R	O/F_L	O/F_R	$\dot{m}_{bb,L}$	$\dot{m}_{bb,R}$
0	81	79	5.7	5.4	4.5	4.4
30	99	100	5.6	5.6	5.4	5.5
60	72	74	5.6	5.7	3.9	4.1
120	69	70	5.3	5.4	3.8	3.9
121	38	39	4.6	4.7	3.2	1.0
240	45	40	6.0	5.9	3.5	1.1

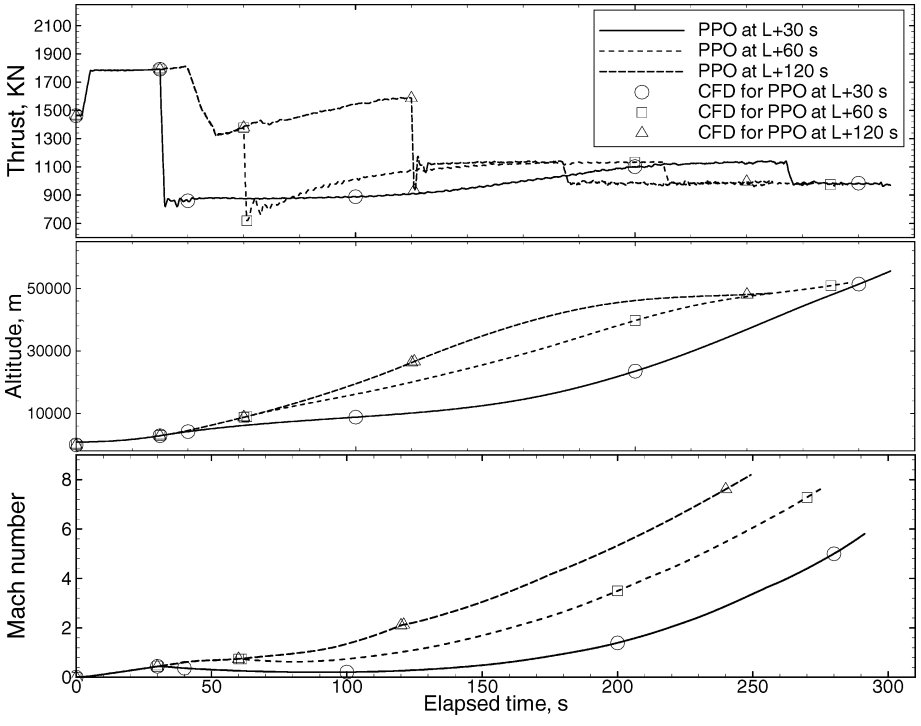

Fig. 6 Thrust, altitude, Mach number profiles, and computational points.

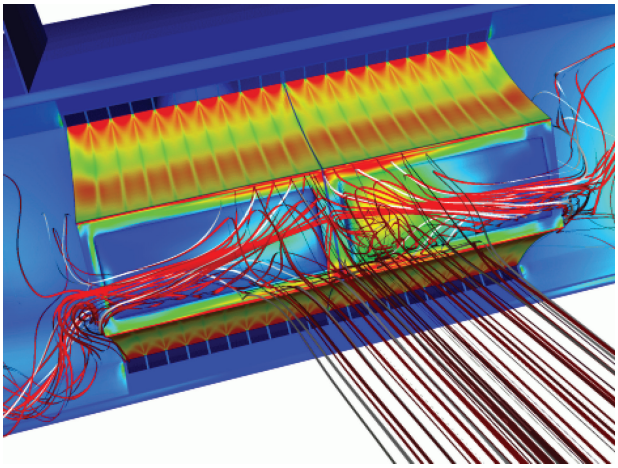

Fig. 7 Convective heat flux contours and streamlines at 40 s into PPO at launch +30-s trajectory; color scales: 0–400 for plug base, 0–9000 for engine ramp, and 0–60 for the rest of the body surface.

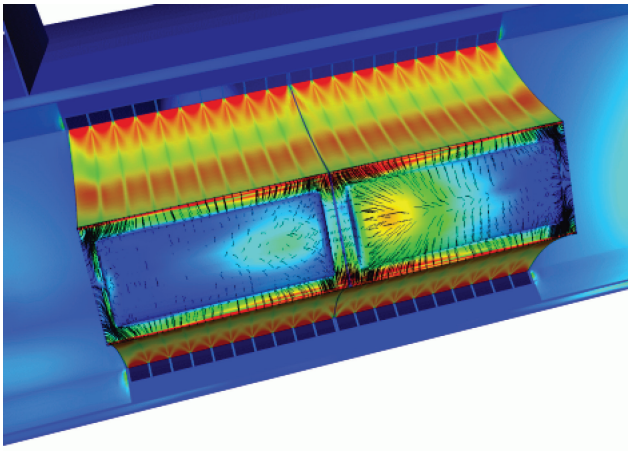

Fig. 8 Convective heat flux contours and surface streamlines at 40 s into PPO at launch +30-s trajectory; color scale identical to that in Fig. 7.

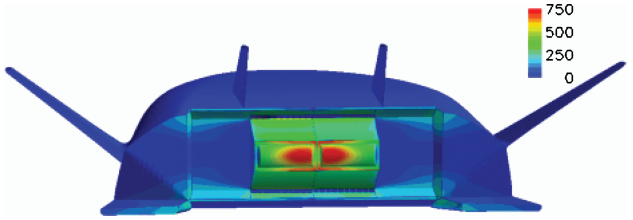

Fig. 9 Radiative heat flux contours at 40 s into PPO at launch +30-s trajectory.

Origin 2000 cluster using 16 processors. The computational time for a typical run is 5.0×10^{-5} CPU s/grid/step/direction/processor. In general, 20–40 iterations are used to achieve an approximately converged solution. Approximate convergence is achieved when all of the residuals dropped at least six orders of magnitude and flow properties monitored at several strategic locations reached steady-state values.

Figure 7 shows the computed convective heat flux contours and streamlines at 40 s into the PPO at launch +30-s trajectory. Figure 7 shows the asymmetric heating pattern where convective heat fluxes are much higher on the plug-base pillow and flex seals of the off-engine side (right side) than those of the on-engine side (left side). For illustration, colored particles are released in streamlines from the flex seals (white) and the pillows (red). The outer streamlines that follow the free shear layers of the two merging engine plumes and plug base form a prism-shaped dome, which enclose the reverse jet and recirculated flow. Eventually, some of the particles following the engine plumes are swept downstream, and some from inside the dome flow laterally on the plug base to become the lateral wall jet.[3,4] Inside the prism-shaped dome and near the center of the plug base, there are extra recirculated flow and reverse jet near the pillow surface of the off-engine side, whereas almost none similar to those above the on-engine side. It is theorized that the low base bleed flow on the off-engine side (Fig. 2) allows the recirculated flow and reverse jet to roam and impinge the surface. On the other hand, higher base-bleed flow on the on-engine side (Fig. 2) pushes the recirculated flow and reverse jet away from the surface. This essentially destroys the recirculated flow and reverse jet, thereby protecting the surface from the hot flow. The low base-bleed flow on the off-engine side also results in a longer residence time for the recirculated flow, increasing the potential of afterburning, which in turn causes higher heating. The recirculated flow and reverse jet leave stronger heating impressions on the plug-base surface of the off-engine side than that of the on-engine side, as demonstrated by the surface streamlines shown in Fig. 8. Figure 8 further shows there are more surface streamlines rolling off the pillow to the flex seals on the off-engine side than those on the on-engine side, indicating higher flex seal heating on the off-engine side. The asymmetric convective heating pattern apparently results from the uneven base bleed.

As power is reduced and altitude increases, the reverse jet weakens and the base convective heating decreases. As a result, the lateral plume jet impingement heating[3] on the outer and offset outer bases also becomes negligible. A similar phenomenon occurs at the two other PPO trajectories. For PPO at launch +120-s trajectory, it appears that the PPO imposes negligible effect on convective base heating due to lower power level and higher altitude at the time of PPO.

Figure 9 shows the computed radiative heat flux contours at 40 s into the PPO at launch +30-s trajectory. The central part of the plug base receives the most radiative heating because the plug base sees the majority of the plume, whereas the ramps receive less. The upper and lower portions of the inner and outer bases receive some radiative heating. The inner and downstream side of the body flap are also affected by the plume radiation, although much less so than that received by the flex seals and pillows. The middle section of the inner and outer bases receives no radiation because the nozzle plug blocks the view. In general, it is found that the computed radiative heat flux after PPO is lower than that before PPO. That is, the effect of reduced power level on radiative heat flux is bigger than that of the reduced base bleed. This is because the volume of the radiating medium affected by the base bleed is much smaller than that of the entire plume. The radiative heating also diminishes with altitudes. Hence, the PPO imposes negligible effect on radiative heating for PPO at launch +120-s trajectory as well.

Figure 10 shows computed centerline convective heat fluxes vs wetted distance in the horizontal direction on various base surfaces of interest for the three PPO scenarios. For clarity, only those at selected trajectory points (before and after PPO) are shown. The centerline heat flux at 0 s is shown in Fig. 10a as a baseline for comparison. At 40 s into the PPO at launch +30-s trajectory and at 50% PL, the peak heating on the off-engine side is higher than that of the on-engine side; it is also higher than those at 0 s (80% PL) and at 30 s (100% PL). This demonstrates the undesirable base-heating effect due to the uneven split of the reduced base bleed that sends only 1.3 kg/s to the off-engine side but 4.1 kg/s to the on-engine side. Note that the highest heating occurs at 0 s between the pillows, indicating some base-bleed protection could be used there. At later times (not shown), for example, at 100 s, although there is still asymmetric heating on the plug base, the absolute magnitude of the heating is less than that before PPO, due to higher plume attenuation. At 200 and 280 s, the plume expansion is too strong to stabilize the special base-bleed boundary condition numerically, and a fixed inlet has to be used, although it can be safely assumed that the convective heating on the pillows at those altitudes is negligible. At 61 s (1 s after PPO) into the PPO at launch +60-s trajectory (Fig. 10b), there is asymmetric heating, and the heating levels are higher than those of the 60 s (before PPO) on both on- and off-engine sides. Because the peak heating level at 61 s is lower than that at

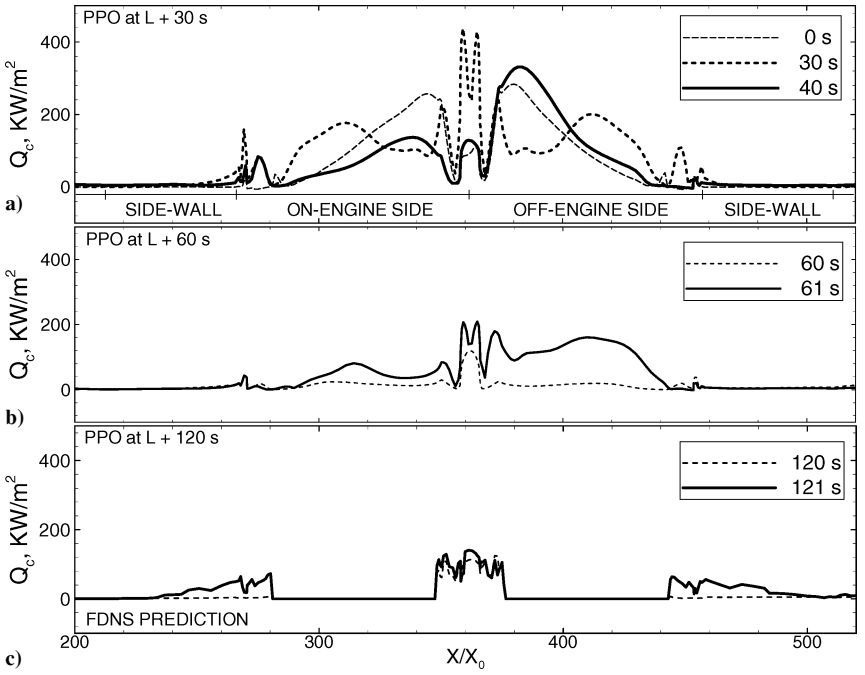

Fig. 10 Effect of PPO on base horizontal centerline convective heat fluxes for three PPO trajectories.

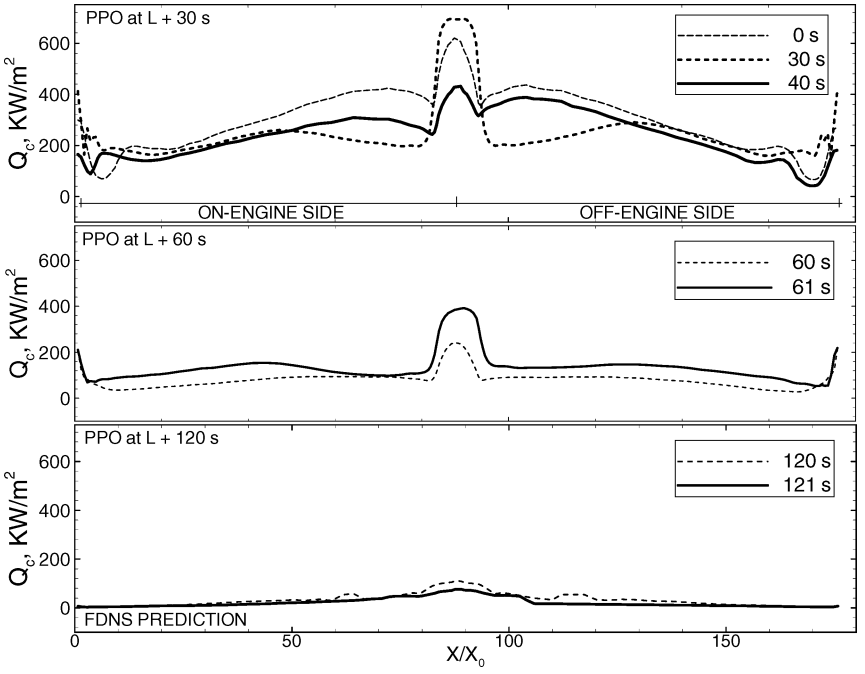

Fig. 11 Effect of PPO on lower flex-seal horizontal centerline convective heat fluxes for three PPO trajectories.

0 s and that at 30 s, it is determined that PPO has negligible impact on plug-base pillow convective heating during PPO at launch +60-s trajectory. Similarly, it can be seen that PPO has negligible impact on pillow convective heating during PPO at launch +120-s trajectory (Fig. 10c) as well.

Figure 11 shows the effect of PPO on the lower flex seal horizontal centerline convective heat fluxes. The heating profiles for the upper and lower seals are slightly different due to the asymmetry of the upper and lower geometries of the X-33 vehicle. Nevertheless, the heating levels for the two seals are very similar, and so only those on the lower seals are discussed. It can be seen that the curves during PPO at launch +30-s trajectory also have distinctive peaks at the center, induced by the strong wall jet created by the reverse jet impingement between the pillows. This wall jet has no place to go but to flow upward (toward the upper flex seal) and downward (toward the lower flex seal), eventually being swiped away by the propulsive flow.[4] The two wings on both sides of the heating curves are induced by the wall jet on the pillows, which moves down the pillow and flows through the seal region. The central heating level of the 30-s curve is higher then that of the 0 s (due to higher engine power level), but its wing heating is flattened out and lower than that of the 0 s (due to higher altitude and more base bleed). At 40 s, although the central heating level is lower than that of the 30 s (due to reduced power level during PPO), its wing heating level is higher and closer to the center (due to reduced base bleed), as well as it is higher at the off-engine side (due to the 75/25 split). The curve at 61 s (after PPO) is higher than that at 60 s (before PPO) in the PPO at launch +60-s trajectory. The curves in the PPO at launch +120-s trajectory are both low, and the effect of PPO is negligible.

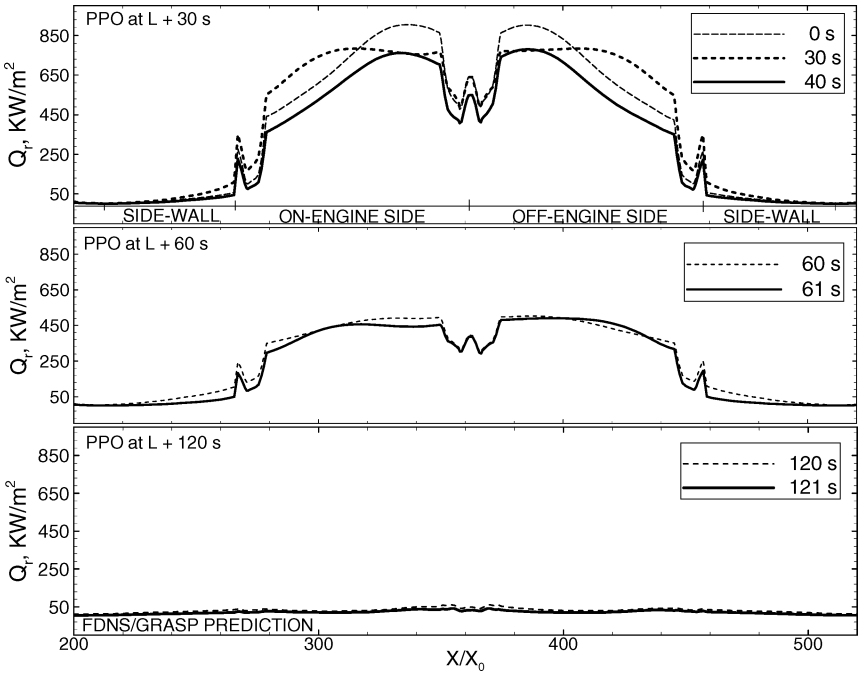

Fig. 12 Effect of PPO on base horizontal centerline radiative heat fluxes for three PPO trajectories.

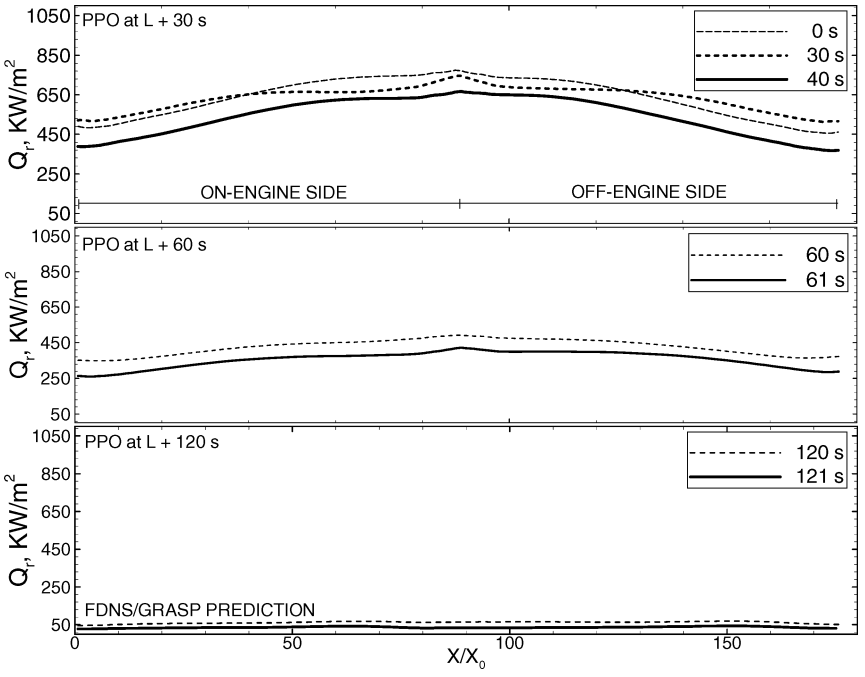

Fig. 13 Effect of PPO on lower flex-seal horizontal centerline radiative heat fluxes for three PPO trajectories.

Figures 12 and 13 show radiative heat fluxes similar to those shown in Figs. 10 and 11 for convective heat fluxes. In addition to the view factor, the radiative heating levels are also functions of power level, altitude, base bleed, and freestream Mach number. Of all of the cases studied, the radiative heating after PPO is mostly lower than or equal to that before PPO on all base surfaces. This is particularly true for the radiative heating on the flex seals. As altitude or PPO time increases, the radiative heating decreases. Note that the level of radiative heating is quite different from that of convective heating on various components. For example, the peak level of radiative heating (Fig. 12) on the base horizontal centerline for PPO at launch +30-s trajectory is about twice as that of convective heating (Fig. 10), whereas the peak heating levels on flex seals for both (Figs. 11 and 13) are about the same. Again, the PPO has no effect on the radiative heating for the PPO at launch +120-s trajectory because the heating level before PPO is already negligible.

Conclusions

A computational heat transfer design methodology was developed to study the linear aerospike plume-induced base-heating environment during PPO in ascent flight. There were 18 ascent trajectory points selected from three PPO scenarios computed. The results are presented as three-dimensional convective and radiative heat flux contours and two-dimensional convective and radiative heat flux profiles vs wetted distance on component surfaces of interest. The base-heating environment during PPO is enveloped, and the dual-engine base-heating physics during PPO is illustrated. In general, the locations enduring the most heating before and after PPO are

the center of the flex seal and the center of the plug base. PPO alters convective base heating most in the earliest scenario (PPO at launch +30-s trajectory). The source of the impact of PPO on base heating comes from the reduced and asymmetric base bleed.

Acknowledgments

John Sutter and Charlie Dill of X-33 Program Office supported this effort. Yen-Sen Chen and Ji-Wen Liu of Engineering Sciences, Inc., provided technical support during the running of the FDNS and GRASP codes. Stan Douglas provided basic trajectory information. Robert Garcia read the memo from which this manuscript is originated. Denise Chaffee produced the streamline plots.

References

[1]Tomita, T., Takahashi, M., Onodera, T., and Tamura, H., "A Simple Performance Prediction Model of Clustered Linear Aerospike Nozzles," AIAA Paper 2001-3560, July 2001.

[2]Huang, D. H., "Aerospike Engine Technology Demonstration for Space Propulsion," AIAA Paper 74-1080, Oct. 1974.

[3]Wang, T.-S., "Analysis of Linear Aerospike Plume-Induced X-33 Base-Heating Environment," *Journal of Spacecraft and Rockets*, Vol. 36, No. 6, 1999, pp. 777–783.

[4]Wang, T.-S., "Effect of Fence on Linear Aerospike Plume-Induced Base-Heating Physics," *Journal of Thermophysics and Heat Transfer*, Vol. 14, No. 4, 2000, pp. 457–463.

[5]Steinbrenner, J. P., Chawner, J. R., and Fouts, C., "Multiple Block Grid Generation in the Interactive Environment," AIAA Paper 90-1602, June 1990.

[6]"Injector Design Tool Improvements—Final Technical Report and User's Manual for FDNS V.4.5," Engineering Sciences, Inc., Rept. ESI-TR-98-02, Huntsville, AL, April 1998.

[7]Liu, J., Shang, H.-M., Chen, Y.-S., and Wang, T.-S., "GRASP: A General Radiation Simulation Program," AIAA Paper 97-2559, June, 1997.

[8]Wang, T.-S., and Luong, V., "Hot-Gas-Side and Coolant-Side Heat Transfer in Liquid Rocket Engine Combustors," *Journal of Thermophysics and Heat Transfer*, Vol. 8, No. 3, 1994, pp. 524–530.

[9]Wang, T.-S., and Chyu, M. K., "Heat Convection in a 180-Deg Turning Duct with Different Turn Configurations," *Journal of Thermophysics and Heat Transfer*, Vol. 8, No. 3, 1994, pp. 596–601.

[10]Wang, T.-S., "Numerical Analysis of Base Flowfield for a Four-Engine Clustered Nozzle Configuration," *Journal of Propulsion and Power*, Vol. 11, No. 5, 1995, pp. 1076–1078.

[11]Wang, T.-S., "Grid-Resolved Analysis of Base Flowfield for Four-Engine Clustered Nozzle Configuration," *Journal of Spacecraft and Rockets*, Vol. 33, No. 1, 1996, pp. 22–29.

[12]Wang, T.-S., and Cornelison, J., "Analysis of Flowfields over Four-Engine DC-X Rockets," *Journal of Spacecraft and Rockets*, Vol. 34, No. 5, 1997, pp. 620–627.

[13]Wang, T.-S., "Delta Clipper-Experimental In-Ground Effect on Base-Heating Environment," *Journal of Thermophysics and Heat Transfer*, Vol. 12, No. 2, 1998, pp. 343–349.

[14]Wang, T.-S., and Chen, Y.-S., "Unified Navier–Stokes Flowfield and Performance Analysis of Liquid Rocket Engines," *Journal of Propulsion and Power*, Vol. 9, No. 5, 1993, pp. 678–685.

[15]Chen, Y.-S., and Kim, S. W., "Computation of Turbulent Flows Using an Extended k–ε Turbulence Closure Model," NASA CR-179204, Oct. 1987.

[16]Wang, T.-S., McConnaughey, P., Chen, Y.-S., and Warsi, S., "Computational Pollutant Environment Assessment from Propulsion System Testing," *Journal of Spacecraft and Rockets*, Vol. 33, No. 3, 1996, pp. 386–392.

[17]Liakopolous, A., "Explicit Representations of the Complete Velocity Profile in a Turbulent Boundary Layer," *AIAA Journal*, Vol. 22, No. 6, 1984, pp. 844–846.

[18]White, F. M., *Viscous Fluid Flow*, McGraw-Hill, New York, 1974, pp. 562, 563.

[19]Liu, J., Shang, H.-M., Chen, Y.-S., and Wang, T.-S., "Prediction of Radiative Transfer in General Body-Fitted Coordinates," *Numerical Heat Transfer*, Pt. B, Vol. 31, No. 4, 1997, pp. 423–439.

[20]Svehla, R. A., and McBride, B. J., "FORTRAN IV Computer Program for Calculation of Thermodynamic and Transport Properties of Complex Chemical Systems," NASA TN D-7056, Jan. 1973.

[21]Frendi, A., Nesman, T., and Wang, T.-S., "Computational and Experimental Study of Linear Aerospike Engine Noise," *AIAA Journal*, Vol. 39, No. 8, 2001, pp. 1485–1492.

[22]Engel, C. D., Bender, R. L., Engel, B. A., and Sebghati, J. M., "NASA SBIR 95-1 Phase II Aerospike Plug Base Heating Model Development Final Report," Qualis Corp., Rept. QTR 017-012, Huntsville, AL, Dec. 1998.

[23]Reardon, J., and Lee, Y.-C., "A Computer Program for Thermal Radiation from Gaseous Rocket Plumes (GASRAD)," REMTech, Inc., Rept. RTR 014-9, Huntsville, AL, Dec. 1979.

Color reproductions courtesy of NASA Marshall Space Flight Center.